JOURNAL OF GEOPHYSICAL RESEARCH, VOL. 113, B09309, doi:10.1029/2007JB005504, 2008

Postseismic displacement of the 1999 Athens earthquake retrieved by the Differential Interferometry by Synthetic Aperture Radar time series

Simone Atzori,[1] Michele Manunta,[2,3] Gianfranco Fornaro,[2] Athanassios Ganas,[4] and Stefano Salvi[1]

Received 16 November 2007; revised 14 April 2008; accepted 24 June 2008; published 18 September 2008.

[1] In September 1999, a moderate (M_w = 5.9) earthquake struck the Attica plain, causing unexpected and extensive damage to Athens and its population. In this work, we exploit the potential of multitemporal Differential Interferometry by Synthetic Aperture Radar (DInSAR) analysis, using about a hundred European Remote Sensing (ERS) 1/2 images to calculate the displacement time series from 1992 to 2002. This analysis allows us to clearly separate a strictly coseismic signal from a postseismic gradual subsidence, reaching a maximum value of about 3 cm in the following 2.5 years. We model this signal in terms of afterslip on the seismogenic fault. The afterslip distribution, retrieved by linear inversion, reflects the coseismic slip distribution and occurs mainly downdip of the area that ruptured during the main shock. The analysis of the static stress transfer suggests that the afterslip was triggered by the main shock, then it propagated aseismically through the fault plane. A partial overlap between the coseismic and aseismic slip area at the hypocentral region indicates that the 1999 rupture surface was not "healed" at least until the date of the last postseismic image (April 2002). The results obtained with a time series approach for this moderate magnitude earthquake suggest that multitemporal DInSAR analysis should become an important methodology for the study of large earthquake ruptures.

Citation: Atzori, S., M. Manunta, G. Fornaro, A. Ganas, and S. Salvi (2008), Postseismic displacement of the 1999 Athens earthquake retrieved by the Differential Interferometry by Synthetic Aperture Radar time series, *J. Geophys. Res.*, *113*, B09309, doi:10.1029/2007JB005504.

1. Introduction

[2] In this work we investigate the full displacement field retrieved by multitemporal Differential Interferometry by Synthetic Aperture Radar (DInSAR) related to the moderate magnitude (M_w = 5.9) 7 September 1999 Athens earthquake. In particular, we exploit the capabilities of time series algorithms to infer the coseismic and postseismic displacement fields. Modeling of the displacement fields gives new insights into the seismotectonic setting and the seismic hazard for the Attica plain and the Athens basin.

[3] Reliability of the standard DInSAR technique in imaging coseismic displacements is well known since the June 1992, M = 7.3 Landers earthquake [*Massonnet et al.*, 1993]. Since 1992, the European Space Agency ERS satellites have provided more than ten years of SAR images, widely used to estimate the coseismic displacement field for almost every large earthquake.

[4] However, DInSAR interferograms are always affected by atmospheric artifacts [*Goldstein*, 1995], usually referred to as Atmospheric Phase Screen (APS), that cannot be easily removed. Intensity and extent of these artifacts can be very variable and the use of analytical models for their compensation is not straightforward, because the needed ancillary data are rarely available [*Li et al.*, 2005]. In the last decade, the abundance of archived ERS images encouraged the development of multitemporal, or "time series", analysis techniques, that combine together dozens of images to retrieve the displacement evolution through time [*Ferretti et al.*, 2000; *Berardino et al.*, 2002; *Mora et al.*, 2003; *Usai*, 2003; *Werner et al.*, 2003; *Hooper et al.*, 2004; *Crosetto et al.*, 2005]. Such approaches allow for mitigation of the APS, assuming that its effect has a statistical correlation in space and decorrelation in time [*Ferretti et al.*, 2000; *Berardino et al.*, 2002]. Moreover, the time series approach allows the calculation of the displacement between two arbitrary acquisitions by a simple difference, overcoming the baseline constraints posed by the standard DInSAR technique [*Gabriel et al.*, 1989]. Multitemporal DInSAR analysis has already shown its potential in retrieving the interseismic

[1] Remote Sensing Laboratory, Istituto Nazionale di Geofisica e Vulcanologia, Sezione di Roma, Rome, Italy.
[2] Istituto per il Rilevamento Elettromagnetico dell'Ambiente, National Research Council, Naples, Italy.
[3] Dipartimento di Ingegneria Elettrica ed Elettronica, Università degli Studi di Cagliari, Cagliari, Italy.
[4] Institute of Geodynamics, National Observatory of Athens, Athens, Greece.

0148-0227/08/2007JB005504$09.00

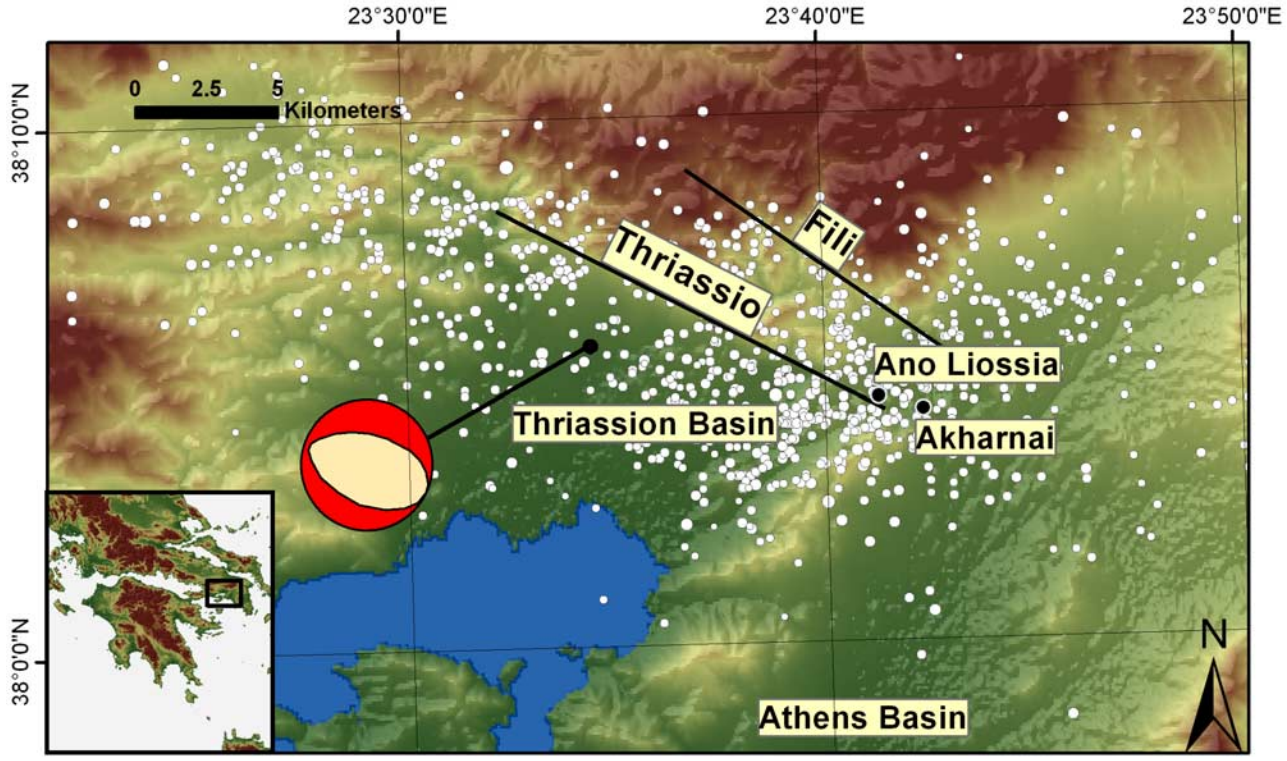

Figure 1. Geographic framework for the 7 September 1999 Athens earthquake. Focal mechanism of the earthquake, aftershock location, known faults, and relevant geographic places are reported.

strain accumulation and postseismic surface motions when high displacement rates are present [*Casu et al.*, 2006; *Fialko*, 2006; *Ryder et al.*, 2007; *Fielding et al.*, 2007].

[5] In this paper we analyze the moderate magnitude Athens earthquake by processing ascending and descending acquisitions from ERS 1 and 2 satellites. We process data using two time series techniques developed at IREA-CNR and we present the results of the inverse modeling of the coseismic and the postseismic signals. The postseismic signal has a very low intensity (about 3 cm in more than 2 years) and can be singled out only by time series techniques, which have shown to be very reliable in the retrieval of low-intensity signals [*Lanari et al.*, 2007].

[6] While many studies exist concerning the modeling of postseismic displacement consequent to a strike slip event [*Bürgmann et al.*, 2002; *Murray and Langbein*, 2006; *Shen et al.*, 1994; *Ryder et al.*, 2007], little literature exists about such modeling on normal faults. Different mechanisms have been proposed to explain postseismic displacement. A first rough approximation [*Marone et al.*, 1991; *Pollitz et al.*, 1998] distinguishes between a short-term afterslip in the upper crust and a long-term viscoelastic relaxation in the lower crust/upper mantle, while poroelastic rebound as a mechanism can be considered also [*Jonsson et al.*, 2003].

[7] Several authors [*Rundle and Jackson*, 1977; *Savage and Prescott*, 1978; *Savage*, 1990] observed how the separation of the afterslip and viscoelastic relaxation mechanisms can be difficult since they predict very similar surface deformation. The analysis gets more complicated when both phenomena act together [*Donnellan and Lyzenga*, 1998]. The static afterslip has been modeled by inversion of elastic solutions [*Donnellan and Lyzenga*, 1998; *Shen et al.*, 1994; *Murray and Langbein*, 2006; *Ryder et al.*, 2007] to infer the slip distribution over some fault plane, but more realistic models are required (e.g., layered earth) when modeling time evolution of the displacement [*Ma and Kusznir*, 1995; *Nostro et al.*, 2001; *Hearn et al.*, 2002; *Hu et al.*, 2004; *Melini et al.*, 2006], invoking viscous or viscoelastic rheologies.

2. Athens Earthquake and DInSAR Data Analysis

[8] The Athens earthquake struck the Attica region of central Greece (Figure 1) on 7 September 1999, with a magnitude M_w = 5.9 (Global CMT catalogue, available at http://www.globalcmt.org/CMTsearch.html; SED, Swiss Seismological Service catalogue, available at http://www.seismo.ethz.ch/; *Louvari and Kiratzi* [2001]). The main shock occurred in a region where no active faults had been mapped [*Papadopoulos et al.*, 2000, 2002]. Despite the moderate size of the earthquake, the macroseismic intensity reached IX in the north-western suburbs of Athens [*Baumont et al.*, 2002]. Because of the soil characteristics and the topographic relief, together with the high density of the population, 145 people died in the collapse of 30 buildings while more than 2000 were injured [*Gazetas et al.*, 2002].

[9] The coseismic displacement field induced by the earthquake was investigated by several authors using a standard DInSAR approach [*Kontoes et al.*, 2000; *Papadopoulos et al.*, 2004; *Baumont et al.*, 2004]. In these studies, several differential interferograms were calculated and the resulting

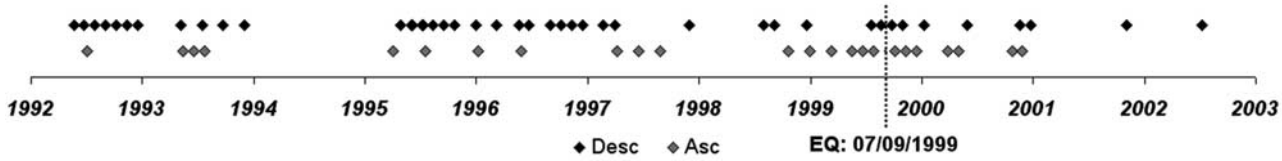

Figure 2. Time distribution of the 26 ascending (track 372, frame 762, gray diamonds) and 47 descending (track 236, frame 2835, black diamonds) acquisitions used for the time series. The dotted line represents the Athens earthquake.

displacement pattern was modeled using various approaches.

[10] For our purposes, we applied two different techniques to obtain the temporal evolution of ground deformation: Small Baseline Subset (SBAS, *Berardino et al.* [2002]) and Enhanced Spatial Difference (ESD, *Fornaro et al.* [2007a, 2007b]), both developed at IREA-CNR, which use different approaches to derive the displacement time series.

[11] SBAS and ESD techniques work on a data set of multilook interferograms in order to detect the spatial low-resolution deformation affecting the area of interest. Moreover, these two approaches estimate and remove the atmospheric artifacts as final step of the DInSAR processing by exploiting the different correlation in space and time of atmosphere and displacement signals [*Ferretti et al.*, 2000; *Berardino et al.*, 2002].

[12] A short summary of the rationale supporting the two techniques is presented in Appendix A; more detailed descriptions can be found in the cited papers.

[13] After the time series generation, we modeled the coseismic and postseismic displacement field; for this purpose, we developed an algorithm to perform linear/nonlinear inversion using input data in slant range geometry and providing the output (fault geometries and slip distribution) in geocoded geometry. We first modeled the fault geometries via nonlinear inversion, then retrieved the slip distribution via linear inversion for the same fault geometries. Finally, we modeled the postseismic signal showing how it can be justified in terms of the afterslip induced by the stress increase which follows the main shock.

[14] We started our processing using 33 ascending images (track 372, frame762) and 66 descending images (track 236, frame 2835) acquired by ERS 1–2 satellites. In the early stage of the processing, some of them were discarded for the excess of missing lines, wrong Doppler centroids or orbital problems. The time distribution of the remaining 26 ascending and 47 descending residual images is shown in Figure 2. Using the constraints of 400 meters of spatial baseline and 1500 days of temporal baseline, we were able to calculate 78 and 170 differential interferograms for the ascending and descending track, respectively. 48 of these interferograms (20 ascending and 28 descending) encompass the September 1999 earthquake and they can thought as "coseismic" (Figure 3).

[15] All the coseismic interferograms of Figure 3 show considerable differences in the fringe patterns, which arise mainly from two causes: the presence of atmospheric artifacts, and/or the existence of some pre- or postseismic displacements. Because of the spatial correlation of the atmospheric signal and the low intensity of the possible pre- or postseismic signal, the mere analysis of the single interferograms does not allow a distinction between these two sources. Time series analysis is the most effective way to combine together the interferograms allowing the filtering, in time, of the atmospheric signal [*Ferretti et al.*, 2000].

3. Data Postprocessing and Modeling

[16] The two time series techniques (SBAS and EDS) allowed for the retrieval of the displacement time evolution for a very high number of points in the Attica plain. Both techniques show the presence of the coseismic displacement and reveal, as will be emphasized later on this paper, the presence of a postseismic trend (Figure 6).

[17] The main difference between the two time series techniques arises from the way the atmospheric artifacts are assessed and removed (see Appendix A), thus affecting the data modeling. We refer, from now on, to the SBAS results, anticipating that the same results were obtained via the ESD technique, indirectly confirming that most of the atmospheric artifacts were correctly removed.

[18] A high degree of spatial correlation is expected in the displacement values retrieved by InSAR and before proceeding to the data inversion, a subsampling of the data sets with a specific algorithm (e.g., the Quadtree algorithm proposed by *Jonsson et al.* [2002]) is advisable.

[19] In our case, for practical reasons due to the slant range geometries of the input data, the number of data points used for the inversion has been reduced using a threshold on the temporal coherence, defined as:

$$\gamma(x,r) = \frac{\left| \sum_{q=0}^{N} exp\left[j\left(\varphi_q(x,r) - \tilde{\varphi}_q(x,r) \right) \right] \right|}{N+1} \qquad (1)$$

where x and r are the azimuth and range coordinates, respectively, $N + 1$ the number of interferograms, $\varphi(\bullet)$ and $\tilde{\varphi}(\bullet)$ the original wrapped and the estimated unwrapped interferometric phases, respectively. Note that the temporal coherence as defined in (1) is always within the [0,1] interval.

[20] We eventually selected ascending and descending data with temporal coherence greater than 0.97 and 0.93, respectively, resulting in about 13000 points for each data set.

[21] Since the temporal coherence decreases with the increase in the number of images, we selected a higher threshold for the ascending data to maintain the data set reliability. Furthermore, a spatial mask in slant range is

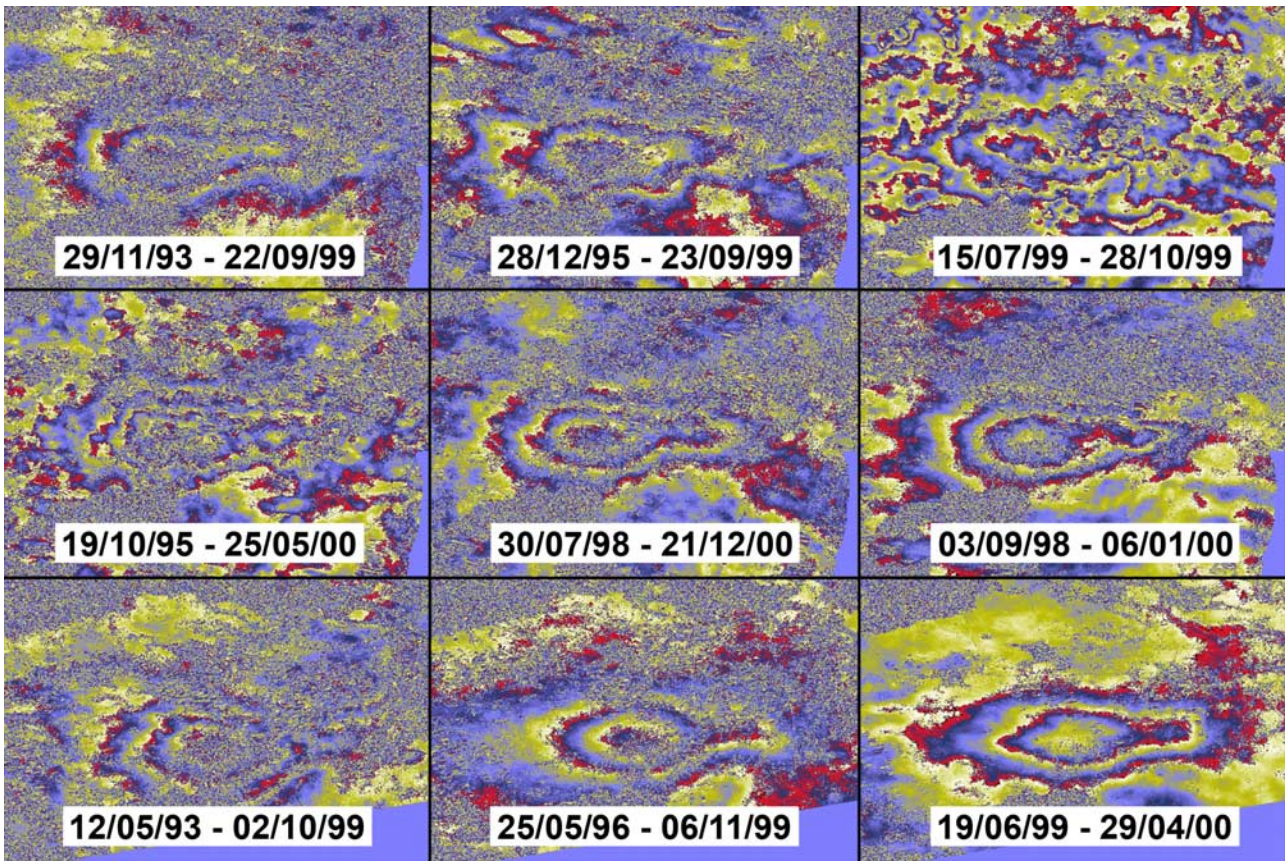

Figure 3. Coseismic DInSAR maps created before the time series generation. In this figure, we show only 9 of the 48 interferograms encompassing the Athens earthquake calculated during the processing. The first two rows are from the descending track, and the last row is from the ascending track. The differences in the fringe pattern are due, basically, to the atmospheric artifacts or to the presence of a preseismic or postseismic signal.

applied to avoid the inclusion of points too far from the earthquake area, potentially affected by a nonseismic signal.

[22] The displacement time series are then referred to the same reference point, chosen in a stable area not affected by any co- or postseismic deformation.

3.1. Coseismic Nonlinear Inversion

[23] Nonlinear inversion is performed to infer the fault geometry from the observed displacement. We use a dislocation model in an elastic half space [*Okada*, 1985] to find the geometries of a fault with uniform slip. The inversion algorithm follows two steps: the cost function is first minimized via Simulated Annealing [*Kirkpatrick et al.*, 1983]; the solution is then refined by a Simplex downhill algorithm [*Nelder and Mead*, 1965].

[24] From the time series we extracted the displacement occurred in the interval 24/07/99-01/10/99 and 19/08/99-22/09/99, for ascending and descending track, respectively (Figures 5a and 5b). Note that classical DInSAR interferograms generated using the same image pairs would be affected by strong spatial decorrelation and unwrapping problems, since their perpendicular baselines are about 600 meters [*Gabriel et al.*, 1989].

[25] We must observe that, although these image pairs isolate at best the coseismic effect, they encompass at least 2 weeks after the earthquake, during which part of the postseismic deformation might have occurred.

[26] We fixed the dip and rake angles using the results by *Baumont et al.* [2004] obtained by joint inversion of SAR and seismological data, applying a correction on the strike angle resulting from the use of the UTM projection. The results of the nonlinear inversion are reported in Table 1; the rms of the residuals is 1.23 cm. Given the uniform slip approximation, length, width and depth of the fault are only indicative; only the fault plane position is retained for the subsequent linear inversion.

3.2. Coseismic Linear Modeling

[27] The linear inversion is performed to retrieve the coseismic slip distribution over the fault with fixed geom-

Table 1. Geometries of the Fault Coming From the Nonlinear Inversion

Length[a] (m)	Width[a] (m)	Top depth[a] (m)	Strike (°)	Dip (°)	Rake (°)	Mean slip (cm)	East[b] (m)	North[b] (m)
7500	3500	11500	110	60	−80	130	732450	4225120

[a]Length, width, and depth of the fault are only indicative since they are kept much larger in the subsequent linear inversion, allowing the slip value to extinguish far from the hypocenter (see Figure 4).
[b]UTM-WGS84, zone 34.

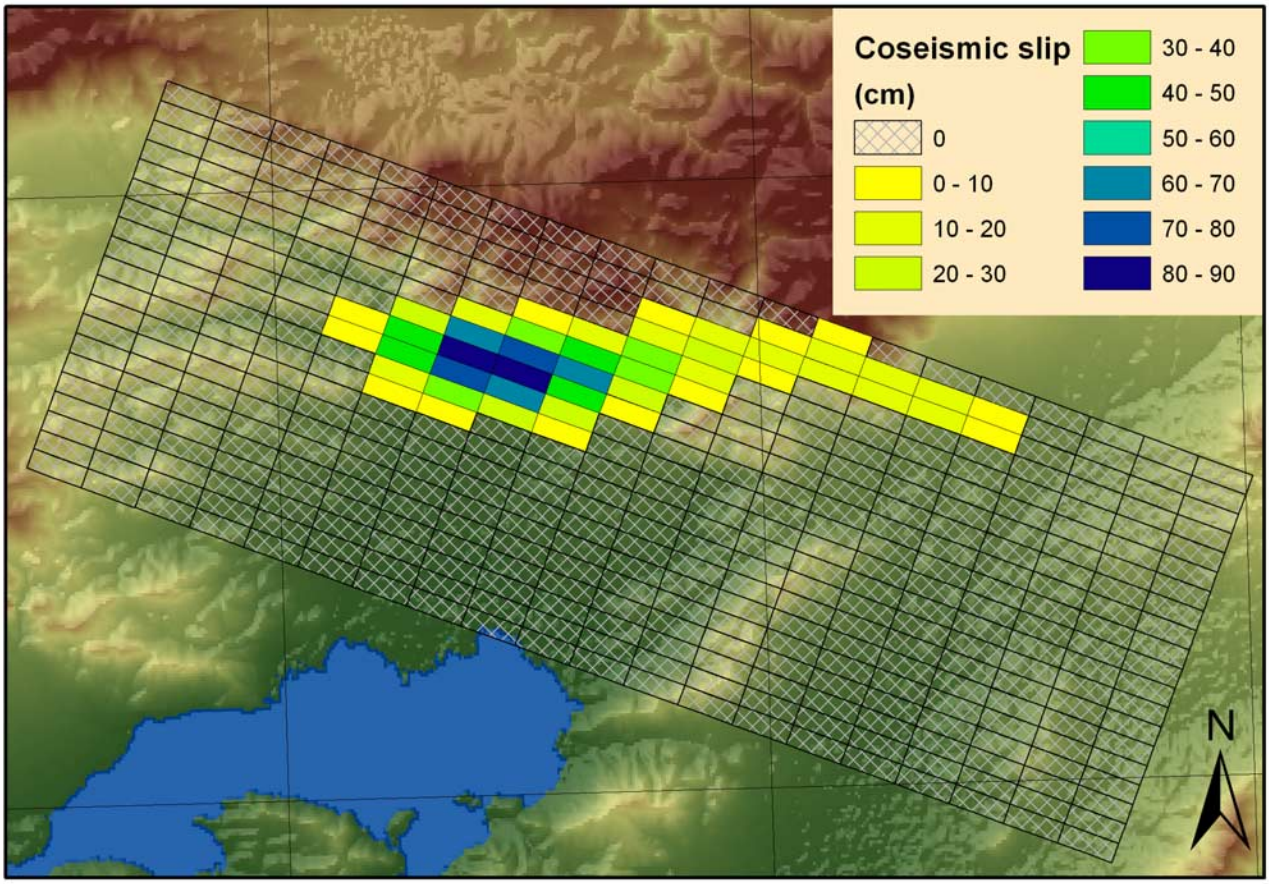

Figure 4. Coseismic slip distribution coming from the linear inversion of the ascending and descending displacement maps of Figure 5. The main fault geometries are retrieved by a nonlinear inversion, with the exception of the length and the width, kept larger than the uniform slip solution of Table 1. For the linear inversion, the fault has been split into 20 × 20 regular patches (1.75 km along strike, 1.25 km along dip). In this geocoded image, the fault is projected on the ground surface.

etries. We first performed a separate inversion for the ascending and descending data set, in order to cross validate the results with independent data set. Then we inverted them jointly to find the best fit slip distribution.

[28] Since we fixed, as previously described, a common reference point, we avoid the inversion for possible map offsets; moreover, the estimate of orbital ramps is not needed, since they are for the most part removed in the time series processing.

[29] The fault plane is split into 20 × 20 patches (Figure 4). The algorithm we use is similar to that described by *Wright et al.* [2003] and *Funning et al.* [2005] and is based on the inversion of the matrix linking the observed data to the model parameter according the following set of equations in a matrix form:

$$\begin{bmatrix} \mathbf{d_a} \\ \mathbf{d_d} \\ 0 \end{bmatrix} = \begin{bmatrix} \mathbf{G} \\ k \cdot \nabla^2 \end{bmatrix} \bullet \mathbf{m} \qquad (2)$$

where $\mathbf{d_a}$ and $\mathbf{d_d}$ are the ascending and descending observed data; $\mathbf{m}$ is the vector of the source parameters (the slip values); $\mathbf{G}$ is the matrix with the Green's functions, expanded to include the Laplacian operator ∇^2, opportunely weighted by the coefficient k, to avoid unrealistic fluctuating solutions. The solution of this equation system is carried out with a Non Negative Least Squares algorithm [*Lawson and Hanson*, 1974], preventing change of direction of the slip across the fault. Projection in the LOS (the Line Of Sight vector of SAR satellites) is carried out taking into account its variability across the scene.

[30] Figure 4 shows the slip distribution retrieved by linear inversion of the coseismic displacement field, while in Figure 5 observed and predicted displacement fields for the ascending and descending tracks are reported. The rms for this solution is 0.51 cm, with a corresponding geodetic moment of $0.78 \cdot 10^{18}$ N·m, equal to that estimated by USGS and slightly lower than that estimated by other institutes (Table 2). Furthermore the slip distribution has a general agreement with that retrieved by other authors [*Baumont et al.*, 2002, 2004; *Roumelioti et al.*, 2003], confirming that only a fault is needed to explain the coseismic deformation.

[31] A peak of about 80 cm is visible in the central part, while the eastward asymmetric extension reflects the presence of an elongation in the slip distribution toward the shallower eastern part of the fault (Figure 4). In this part, the dislocation has a mean value of 20 cm. The maximum slip has a depth of 8.5 km, which is the expected depth of the hypocenter (Table 2).

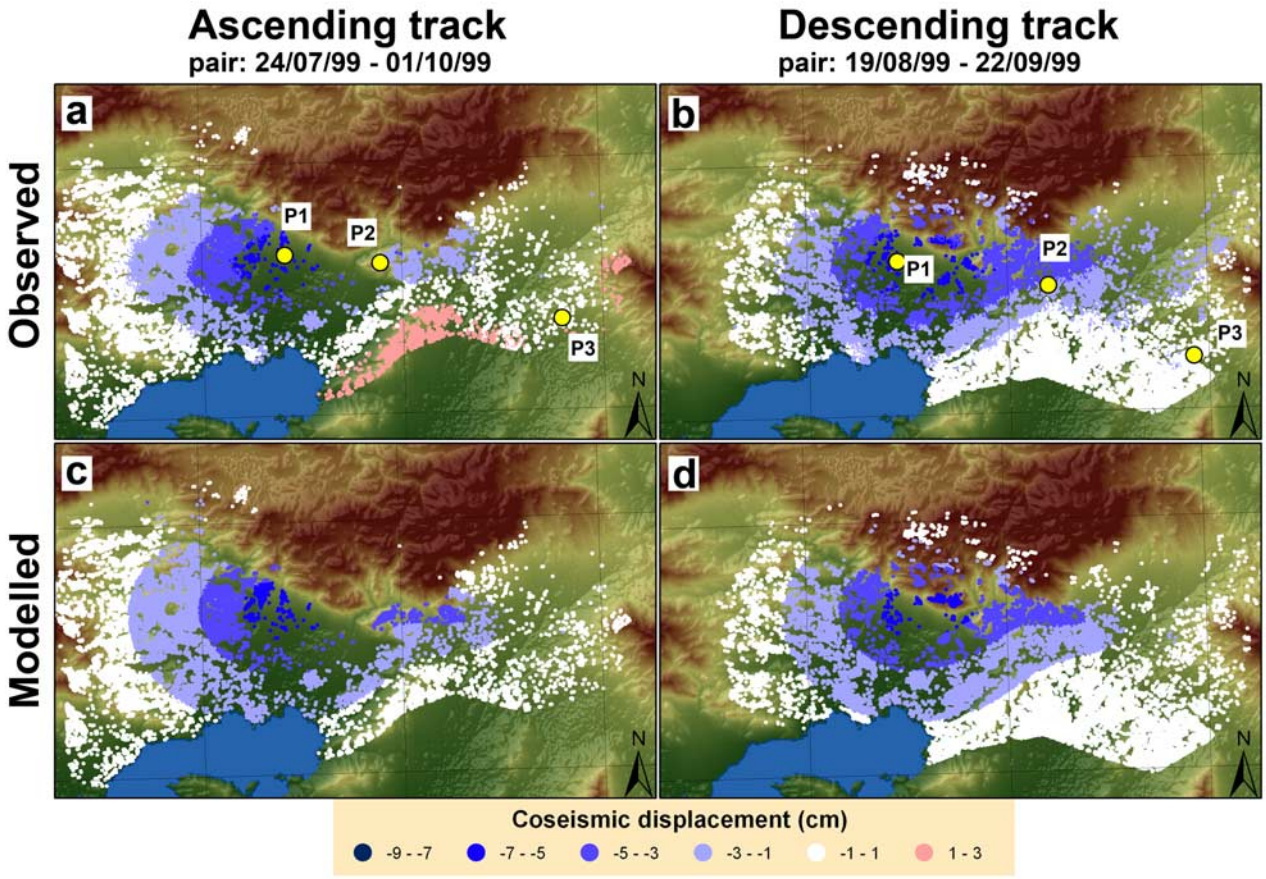

Figure 5. Observed and modeled coseismic displacement maps for the (a and c) ascending and (b and d) descending tracks. The observed displacements are calculated by subtracting the last preseismic to the first postseismic acquisition (pairs 24 July 1999 to 1 October 1999 and 19 August 1999 to 22 September 1999 for the ascending and the descending tracks, respectively). Such pairing would be impossible with a standard DInSAR approach because of the excessively large perpendicular baseline. The modeled displacement fields (c and d) are calculated with the elastic solution of *Okada* [1985] applied to the coseismic slip distribution of Figure 4. The yellow squares P1, P2, and P3 represent the locations associated with the time series shown in Figure 6.

[32] For a detailed description of the approach and the results of the uncertainty assessment on the slip distribution, see the Appendix B.

3.3. Postseismic Linear Modeling

[33] After the linear modeling, we subtracted the predicted coseismic displacement from the time series (e.g., from each acquisition after the earthquake). We then carried out the APS filtering (essentially low-pass in time, see Appendix A) on the time series, thus overcoming the problems of a temporal smoothing of the coseismic step. As a consequence of the filtering we were able to emphasize the presence a postseismic signal.

[34] In Figure 6 we report, for three points representative of the entire area, the raw time series, before the removal of the coseismic step and the APS filtering, and those in which the signal has been cleaned from the coseismic contribution and filtered in time. The subsidence trend, starting after the September 1999 earthquake, is evident. As we move away from the epicenter (from point P1 to P3 in Figures 5a and 5b),

Table 2. Focal Mechanism for the Athens Earthquake From Several Institutes and Authors

Longitude (deg)	Latitude (deg)	Depth (km)	Strike (deg)	Dip (deg)	Rake (deg)	M_0 10^{18} N·m	Institute or author
23.55	38.02	9.0	123	55	−84	0.78	USGS-NEIC
23.64	37.87	15.0	116	39	−81	1.14	Global CMT catalog
23.55	38.13	12.0	102	47	−79	1.18	SED
23.54	38.06	10.0	115	57	−80	0.92	*Louvari and Kiratzi* [2001]
23.58	38.08					0.57	*Stavrakakis et al.* [2002]
		10.0	115	60	−80	0.60	*Sargeant et al.* [2002]
23.58	38.08	16.8	113	39	−90		*Papadopoulos et al.* [2000]
23.58	38.12	9.5	112	60	−84	1.6	*Baumont et al.* [2004]

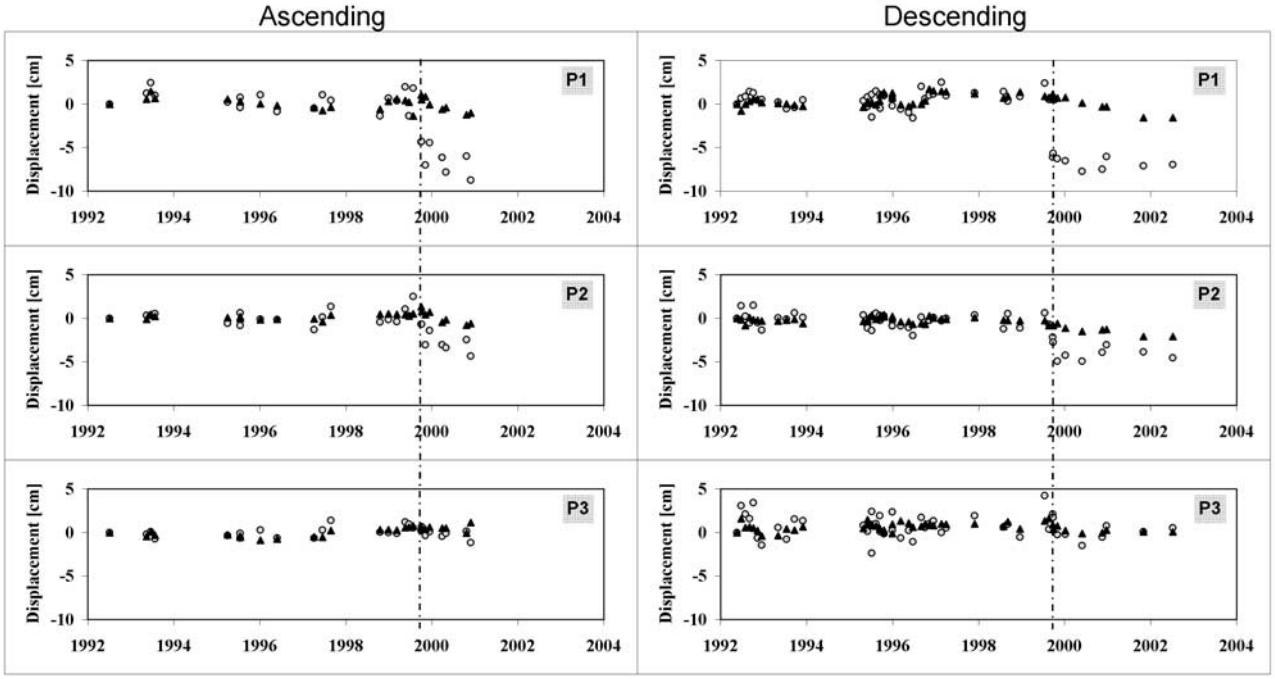

Figure 6. (right) Descending and (left) ascending time series for three points at different distances from the epicenter (see the location of P1, P2, and P3 in Figures 5a and 5b). White circles represent the raw time series before the filtering of atmospheric artifacts and the removal of the coseismic "step." Black triangles represent the time series after the modeling of the atmospheric artifacts and the removal of the modeled displacement. The dotted line indicates the September 1999 seismic event. Note that the availability of a larger descending data set allows for the retrieval of a more evident signal; however, the earthquake discontinuity and the postseismic trend are visible with both orbits.

the intensity (slope) of this subsidence gets lower, tending to gradually disappear.

[35] The postseismic trend is more evident for the descending track, since the longer period of observation after the earthquake (2.5 years in descending mode, 1 year for the ascending). Furthermore, the higher number of images compared with the ascending track (47 images vs. 26) allows for a better filtering of the APS and the retrieval of a more stable solution. From the same plots we observe the absence of a significant preseismic signal.

[36] This led us to calculate and model, only for the descending track, the displacement that occurred between the first postseismic image (22/09/99) and the last image of the time series (04/04/02). This map shows that the subsidence in the Thriassion basin doesn't exceed 3 cm in about 2.5 years after the earthquake (Figure 8a).

[37] As discussed in the introduction, we modeled this data in terms of afterslip, triggered by the dislocation of the September 1999 main shock. We considered also the possibility of other nontectonic causes, like water pumping and/or groundwater flow, as well as the presence of fluid migration induced by the earthquake itself. In both cases the temporal behavior of the displacement is not supporting these hypotheses. In fact, water table fluctuations are often periodic, while the effect of fluid migration as a consequence of the earthquake should vanish a few weeks after the event [*Husen and Kissling*, 2001]. The analysis of the temporal behavior led us to further reduce the number of observed points in the eastern part of the plain.

[38] We used the algorithm described in the previous section to retrieve the slip distribution shown in Figure 7. The total seismic moment calculated in terms of afterslip is $0{,}38 \cdot 10^{18}$ N·m, that is 49% of the seismic moment released by the main shock, according to the USGS. The rms between the predicted and observed displacement is 0.23 cm.

4. Coulomb Stress Increase as Origin of the Afterslip

[39] Our work shows that the 1999 earthquake triggered afterslip along the fault plane with a major fraction in the downdip direction from the main rupture (Figure 7). The remaining fraction occurred along strike (i.e., bilateral): no up-dip afterslip was observed. This is in agreement with the absence of seismicity at shallow depths (<2 km) reported from the portable seismological networks. We calculated a ruptured area of 102.8 km^2 and an afterslip area of 146.5 km^2 or about 42% greater. In total, there is a 44% overlap between seismogenic and aseismic regions of the fault mainly in the hypocentral area (6–10 km depth). 20% of that overlap (about 11 km^2) refers to areas where afterslip exceeded co-seismic slip, while maximum afterslip occurs immediately downdip from the maximum slip. The amount of overlap suggests that nearly half of the coseismic slip area has not "healed" for at least 2.5 years after the main shock. At the depth of 9–10 km afterslip magnitude is the highest (30 cm) implying that the mean afterslip rate was about 0.3 mm/day ($\Delta T = 925$ days for the descending track) although this displacement may have accumulated faster

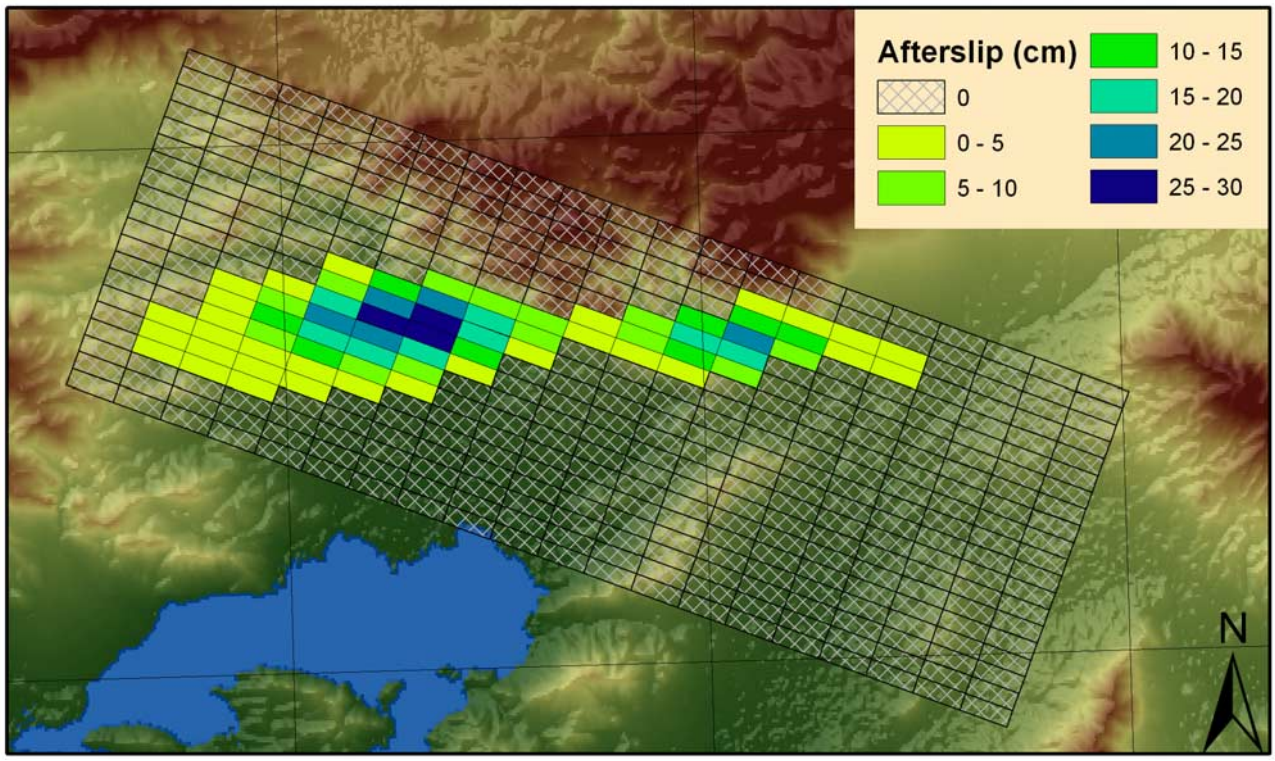

Figure 7. Slip distribution retrieved by linear inversion of the postseismic displacement field calculated from the descending time series. The fault geometries and its subdivision in patches are the same as those of Table 1 and Figure 4. The afterslip represents the distributed dislocation cumulated in the 2.5 years after the Athens earthquake; our analysis shows the strong correlation with the coseismic slip distribution of Figure 4 through the stress transfer modeling.

during the first few months after the earthquake, as can be inferred by inspecting the time evolution of the displacement for some points (Figure 6).

[40] We suggest that the afterslip occurred because of static (Coulomb) stress increase downdip of the rupture patch. To show this correlation we calculated Coulomb stress changes using the coseismic slip distribution resulting from the linear inversion (Figure 4). The coseismic slip patches were modeled as rectangular dislocation elements on an inclined slip surface. We used the DLC code [*Simpson and Reasenberg*, 1994], based on the dislocation modeling for a homogeneous, elastic half space [*Okada*, 1985]. Table 3

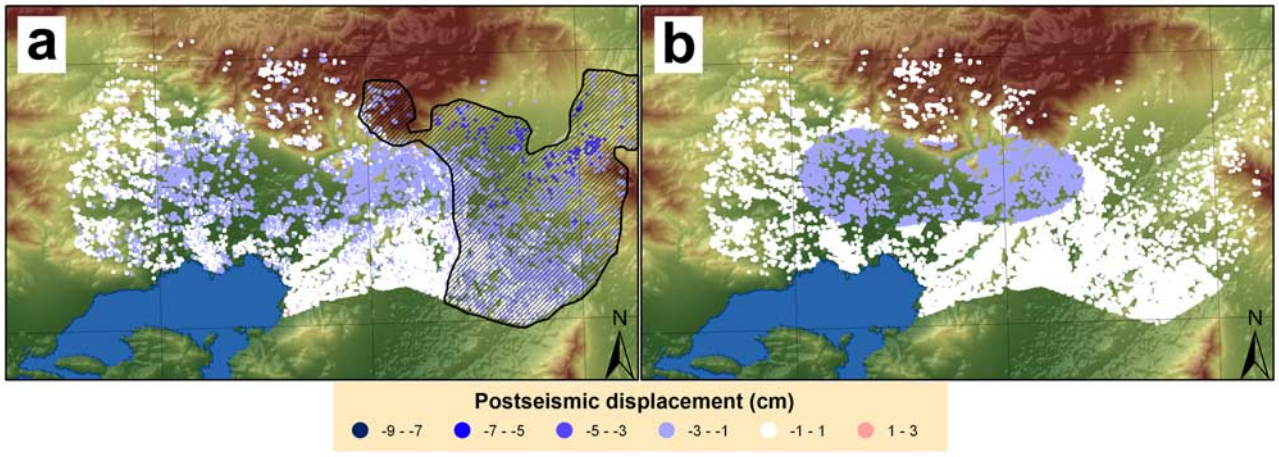

Figure 8. Postseismic displacement (a) observed and (b) modeled retrieved from the descending time series in the interval 22 September 1999 to 4 April 2002. The modeled displacement field corresponds to the afterslip distribution of Figure 7. We discarded points affected by a long-term displacement not correlated with the postseismic trend (shaded area). These points can be easily detected by visual inspection of the relative time series.

Table 3. Input Parameters for Stress Transfer Modeling

Poisson ratio	0.25
Shear modulus	30 GPa
Coordinates of centre of ΔCFF grid	Lat 23.624°, Lon 38.087°
Depth of centre of ΔCFF grid	10 km
Patch size (km)	1.75 km (along strike), 1.25 km (along dip)
Friction coefficient	0.4
Slip Model	Linear inversion (47 coseismic patches, see Figure 4)

summarizes our modeling parameters. The stress changes are applied to a "fixed" receiver plane using the same geometry and kinematics as the coseismic case: strike is N110°E, dip is 60 degrees to the south and the rake angle is −80° (Table 3). The Coulomb failure criterion used is [*Harris*, 1998]:

$$\Delta\mathrm{CFF} = \Delta\tau + \mu' \cdot \Delta\sigma_n \quad (3)$$

where ΔCFF is the Coulomb stress (positive for encouraging failure), $\Delta\tau$ is the change in shear stress on the receiver fault (positive in the slip direction), μ' the effective (or apparent) coefficient of friction incorporating fluid pore pressure changes and $\Delta\sigma_n$ is the change in normal stress acting on the receiver fault (with extension positive). μ' is treated as constant in this study with a value of 0.4 which is considered as appropriate for mature faults [*Harris and Simpson*, 1996; *Harris*, 1998]. First we compute the stress tensor along a 60-degree inclined grid due to the coseismic dislocations (slip distribution shown in Figure 4). We obtain 6 grids, one for each tensor component. After that, we compute ΔCFF on the "receiver" fault, that is a plane of fixed orientation which is likely to provide the plane of failure. All calculations assumed a Poisson's ratio of 0.25 and a shear modulus of 3 $*10^5$ bar for the elastic upper crust.

[41] Our results are shown in Figure 10 where the centers of slip patches are superimposed on the map of Coulomb stress. The map shows areas where slip is promoted because of large increase in ΔCFF approaching 7 bar; areas where slip is suppressed are shown with negative values. To further support this conclusion we overlay the 47 center-points of the coseismic slip elements on the ΔCFF grid (shown as yellow triangles) as well as the earthquake hypocenter of *Baumont et al.* [2004]. Both items correlate well with ΔCFF-relaxed areas. We infer that our modeling was able to satisfactorily reproduce the stress field following the 7 September 1999 earthquake. In addition, the loaded areas (shown with reddish color in Figure 10) extend to a distance approximately 6–8 km away from the coseismic slip boundary. Less increased stress occurs on the eastern (right) area of the rupture. The asymmetry in the loaded area pattern reflects the amount of coseismic slip resolved along each dislocation element. We then overlay the centre-points of the 67 postseismic patches (Figure 7) shown here as green boxes. Spatial correlations between the changes in Coulomb stress and location of postseismic patches are evident.

[42] Moreover, the distribution of the 1000 + aftershocks recorded by the NOA portable network (Figure 9) clearly match the stress-loaded area surrounding the fault plane (Figure 10), however noting, that the seismological data were collected early in the postseismic cycle (first two months after 7 September 1999).

5. Seismotectonics Setting and Implication for the Seismic Hazard

[43] A seismotectonic analysis of this earthquake shows that the surface projection of the modeled fault plane (Figure 4) intersects the Thriassion normal fault (Figure 1) and crosses the surface near the outcropping Fili Fault in agreement with seismological data [*Papadopoulos et al.*, 2000; *Tselentis and Zahradnik*, 2000; *Sargeant et al.*, 2002], geological data [*Pavlides et al.*, 2002; *Ganas et al.*, 2004] and numerical simulations [*Papadopoulos et al.*, 2004]. In fact the limestone ridges comprising the footwall of Thriassion fault have subsided by an amount of 5 to 7 cm (descending pair; Figure 5b). However, our results also suggest that the SE segment of the Fili fault (segment 4; *Ganas et al.*, 2004) did not rupture during the 1999 earthquake, as the surface subsidence field extends in the footwall area of this segment. This observation indicates that only the NW segments of the Fili fault have been activated during the 1999 earthquake. Those segments have a more easterly strike and they join at depth onto a seismogenic plane with a strike direction between 110–120 degrees (clockwise from North).

[44] Our modeling also shows that a few cm of coseismic slip nearly reached the surface toward the SE termination of the rupture (depth to top patch 860 m). In the same area we observe coseismic subsidence of the Earth surface on the order of 1 to 5 cm (municipalities of Ano Liossia and Acharnai; Figure 5). This effect is due to fault rupture becoming shallower as it dies out inside the Athens basin (Figure 4). The tip of the rupture is located about 2 km to the west of the Kifissos river banks where much damage was recorded [*Gazetas et al.*, 2002; *Assimaki et al.*, 2005]. In addition, it is unlikely that the 3 km long shallow patch of the slip plane retrieved from inversion (Figure 4) represents a newly formed rupture. The most likely scenario is that this narrow patch was created (on a pre-existing plane) by a combination of two factors: (1) the strong SE directivity effect of the rupture [*Roumelioti et al.*, 2003] which relates

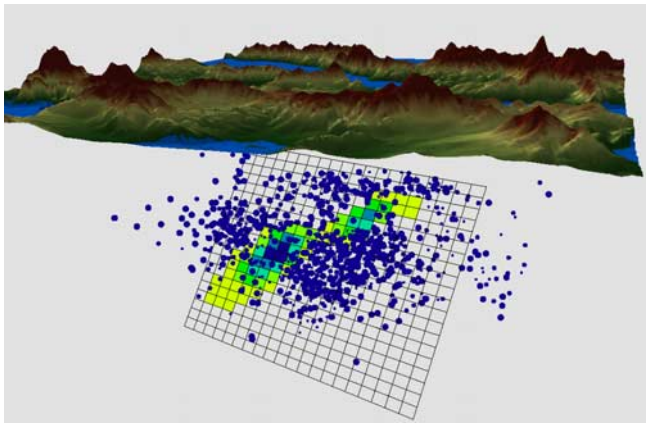

Figure 9. 3D view of the aftershock distribution recorded between 8 September 1999 and 29 October 1999, compared with the afterslip inferred from the linear inversion of the postseismic displacement.

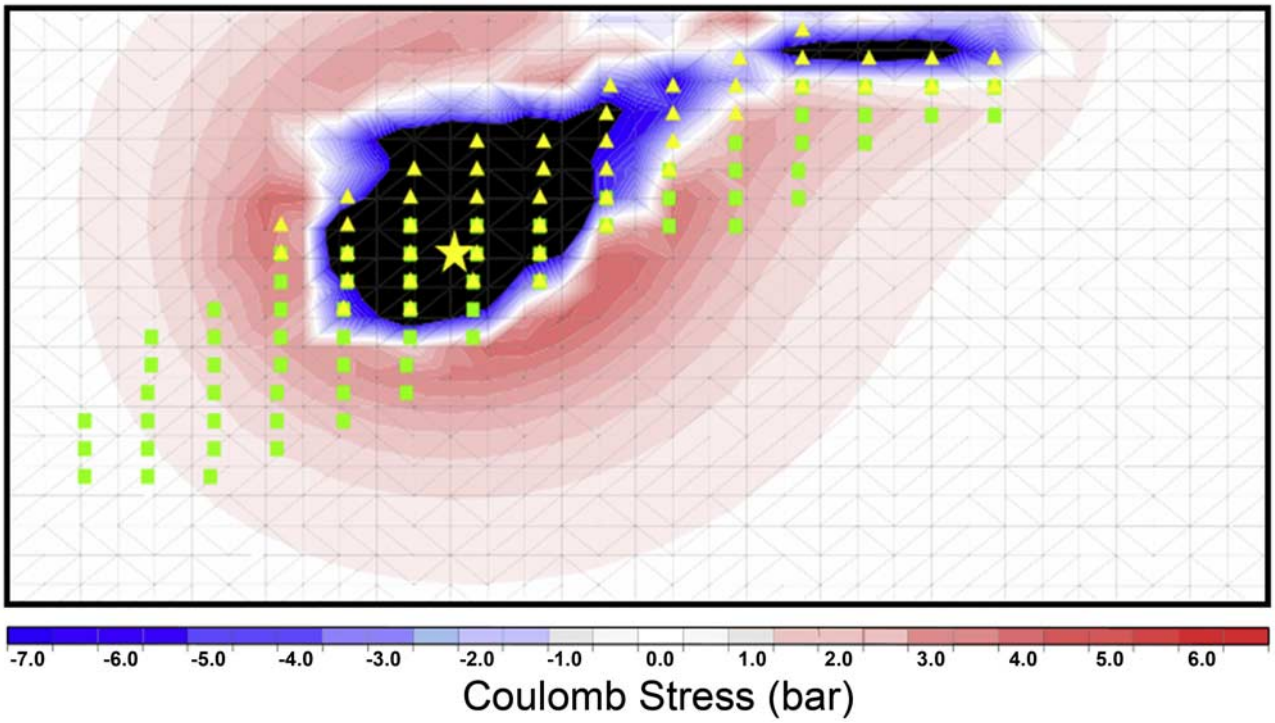

Figure 10. Map of coseismic Coulomb stress changes on the fault plane; red indicates positive stress change, blue the opposite. The coefficient of friction is 0.4. ΔCFF calculation on Athens-type receiver normal fault plane assuming the linear inversion rupture model. Coseismic slip patches and afterslip patches are indicated by yellow triangles and green boxes, respectively. For modeling parameters, see Table 3.

to the dynamics of the rupture and (2) the existence of an asperity at deeper levels. This would imply that the seismogenic structure ruptured in 1999 continues at depth inside the Athens basin beneath Ano Liossia and Acharnai, crossing at ~right angle the bedrock ridges of both Parnitha and Egaleo mountains. Such issue has obviously serious implications for the seismic hazard assessment of the strongly populated urban area of Athens, and needs to be investigated in greater detail.

6. Conclusions

[45] Our results showed how DInSAR time series techniques improve the quality and reliability of the coseismic displacement retrieval. Our solution for the coseismic slip distribution confirms the results presented in previous works [*Kontoes et al.*, 2000; *Papadopoulos et al.*, 2004; *Papadimitriou et al.*, 2002; *Baumont et al.*, 2002; *Roumelioti et al.*, 2003], although a joint inversion of SAR and broadband data [*Baumont et al.*, 2004] is needed to improve its spatial resolution.

[46] The DInSAR time series analysis has the major advantage of detecting and discriminating between subtle pre- or postseismic signal. For the 1999 Athens earthquake we were able to extract from the descending track, a postseismic displacement of about 3 cm in 2.5 years. In such analysis, a large image data set improves the filtering out of the APS contribution.

[47] We interpreted and modeled the observed postseismic displacement field in terms of afterslip, rejecting other possible causes. We mapped an afterslip equivalent to a M_w = 5.68 event in the period 22 September 1999 to 4 April 2002. The dislocation occurred mainly downdip of the area that slipped during the main shock. The overall pattern of afterslip reflects the coseismic slip distribution along the fault plane. The correlation between positive Coulomb stress increase and location of afterslip suggests that afterslip occurred because of the sudden stress load imposed coseismically on the lower part of the fault plane.

Appendix A: Time Series Algorithms

A1. The SBAS technique

[48] The SBAS technique [*Berardino et al.*, 2002] is a DInSAR approach that relies on the use of a large number of SAR acquisitions and implements an easy combination of a properly chosen set of multilook DInSAR interferograms computed from these data, finally leading to the generation of mean deformation velocity maps and displacement time series. In this section, we highlight what are the key issues of the algorithm and refer to *Berardino et al.* [2002] for a more detailed analysis.

[49] First of all, the data pairs used to generate the multilook interferograms are characterized by a small separation (baseline), both in time and space, between the orbits of the SAR acquisitions in order to limit the noise effects usually referred to as decorrelation phenomena. This pairs selection leads to preserve the temporal and spatial coherence characteristics of the interferograms improving the spatial density of the reliable points.

[50] The original phase signal of each interferogram is retrieved by an unwrapping operation based on the minimum cost flow algorithm [*Pepe and Lanari*, 2006], integrated with a region growing procedure to get better performances in areas with low signal to noise ratio.

[51] In order to increase the number of the available SAR acquisitions, i.e., to better follow the temporal trend of the displacement phenomena, data set separated by large spatial and/or temporal baselines are "linked" by applying the Singular Value Decomposition (SVD) method.

[52] Finally, by exploiting the space–time information, atmospheric artifacts are filtered and removed from the displacement information. In particular, this filter step is implemented by exploiting the high correlation in space but poor in time of the atmospheric phase signal. Accordingly, these undesired signals are identified via the cascade of a low-pass filtering, carried out in the two-dimensional spatial domain, followed by a temporal high-pass filtering. This operation also allows us to detect possible orbital ramps caused by inaccuracies in the SAR sensors orbit information. Following their identification, the atmospheric artifacts and the orbital ramps are finally removed.

[53] As a result of the SBAS algorithm, we can generate spatially dense deformation maps and produce deformation time series for each coherent pixel identified in the imaged scene.

A2. ESD Technique

[54] The Enhanced Spatial Differences (ESD) works out multilook differential interferogram stacks to achieve a large coverage, similarly to the SBAS technique; however it extensively exploits spatial differences, i.e., pixel to pixel variations during the processing. More specifically, the algorithm is characterized by the presence of a processing step that carries out a multibaseline/multitemporal unwrapping by assuming a linear model for the deformation signal. This step is implemented by considering pixel to pixel variations of the phase signal to efficiently tackle the atmospheric contribution during the multipass analysis. The result of this step is an estimate of the pixel to pixel variation of the residual topography and mean deformation velocity, which are subsequently spatially integrated in a weighted Least Square sense. The output of the integration step provides a pre-estimate of the mean deformation velocity and residual topography for each pixel. Such signals are used to improve the subsequent unwrapping of each differential interferogram that, after a regularized inversion in the time direction similar to the original SBAS approach, leads to the determination of the time series of the coherent targets.

[55] In the filtering of the data used in this work ESD uses, for the atmospheric filtering of time series, a solution able to preserve temporal discontinuities associated to coseismic signal; this is achieved via a median filter, widely used in edge preserving image filtering. The filtering can be applied to the time series provided by any multitemporal algorithm, without invoking the modeling of the coseismic displacement at this stage. The median filter is available in many software environments, although it may be easily implemented by evaluating the median value on a slicing temporal widow via a simple sorting. It should be stressed that, because of the irregular temporal sampling nature of the time series and because of the fact that the sorting operation must be symmetrical in terms of samples around the output filtered instant, the temporal length of the filtering is inherently non stationary.

[56] The ESD technique has been tested to monitor wide areas: details of the algorithms are provided by *Fornaro et al.* [2007a, 2007b].

Appendix B: Uncertainty Assessment of the Slip Distribution

[57] The slip distribution retrieved by linear inversion, both coseismic and postseismic, provides the best fit values in a least square sense; observed data, however, are affected by uncertainties that reflect in the precision of the estimated parameters. We present the way we used to assess how uncertainties are mapped from the observed data to the predicted model, taking into account the high degree of correlation affecting DInSAR data. Starting from the relation $\mathbf{d} = \mathbf{Gm}$, we find the inverse generalized $\mathbf{G}^{-g}$, via SVD, through which we estimate the model parameters:

$$\mathbf{m}_{est} = \mathbf{G}^{-g}\mathbf{d} \tag{B1}$$

that represents the least square solution already described in the section 3.2.

[58] Since the linearity of the problem, and assuming that the data covariance matrix [cov **d**] is known, we have [*Menke*, 1984]

$$[\mathrm{cov}\mathbf{m}] = \mathbf{G}^{-g}[\mathrm{cov}\mathbf{d}]\mathbf{G}^{-gT} \tag{B2}$$

where [cov **m**] is the $N \times N$ covariance matrix of the model parameters (where N are the 400 slip values, in this study).

[59] The $M \times M$ matrix [cov **d**] (where M is the number of observed points) has the variance (assumed equal for all the points) in the diagonal, and the covariance between points in the off-diagonal. If we assume that the covariance can be expressed as a 1-D function of the distance between points [*Hanssen*, 2001], it can be modeled by analyzing the autocorrelation function of an interferogram containing only correlated noise and no displacement signal. Using an approach similar to that described by *Parsons et al.* [2006], we used a tandem pair (i.e., a pair of images with 1-day of temporal baseline) finding the covariance/distance distribution of Figure B1. It is worth remembering that the 1-day interferogram comes from the difference between the two displacement maps in the time series and not from the standard DInSAR processing.

[60] Four tandem pairs were analyzed, allowing the definition of the following function to describe the covariance of correlated noise:

$$f(r) = \frac{\sigma_S^2}{(a \cdot r + 1)} \cdot \cos(b \cdot r) \tag{B3}$$

where σ_S^2 is the variance (e.g., the covariance at zero distance), r is the distance and a and b are two empirical parameters. The parameter a describes how "fast" the correlation decreases with the distance; the $\cos(b \cdot r)$ function allow the modeling of a negative correlation, present in this area.

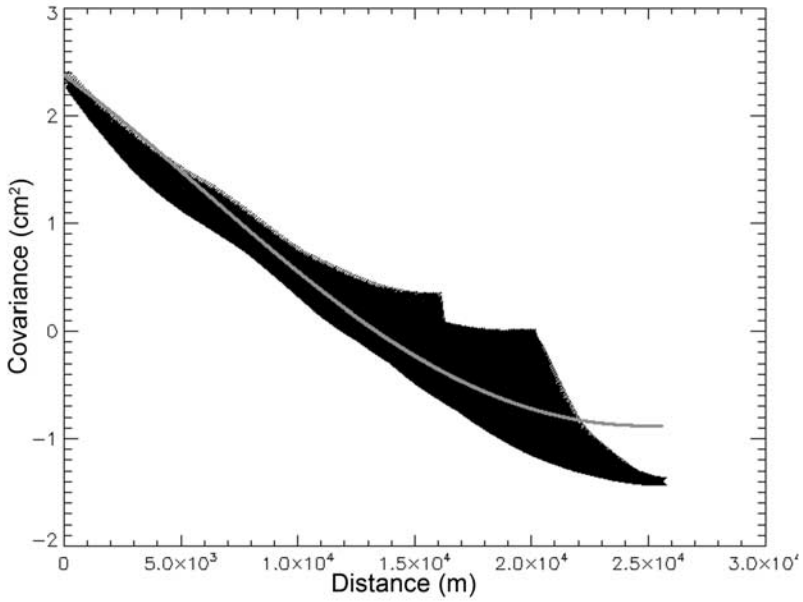

Figure B1. Covariance (cm^2) vs. distance (m) distribution derived from the autocorrelation analysis of the pair 05 July 1995 to 6 July 1995. This pairing is obtained as a difference between the two acquisitions in the time series and must not be confused with the corresponding DInSAR tandem pair. The gray curve describes the "best fit" functions of equation (6). This analytical function is used to generate spatially correlated noise as described by *Parsons et al.* [2006].

[61] The calculation of the [cov **m**] matrix starts from the $M \times M$ matrix with the distances between the observed points; then, we apply equation (6) to obtain the symmetric matrix [cov **d**] for equation (5).

[62] The covariance matrix for the model parameters is a $N \times N$ symmetric matrix of the type

$$[\mathrm{cov}\mathbf{m}] = \begin{bmatrix} \sigma^2_{m1} & \sigma_{m1,m2} & \cdots & \\ \sigma_{m2,m1} & \cdots & & \sigma_{mN-1,mN} \\ \cdots & \sigma_{mN,mN-1} & \sigma^2_{mN} & \end{bmatrix}$$

where σ^2_{mi} is the variance of the slip values for the i-th patch, and $\sigma_{mi,mi}$ are the covariance between the i-th and j-th patches.

[63] Strong correlation exists between the slip values and neglecting these trade-offs lead to an overestimate of the uncertainties of the **m** vector. To obtain a more realistic value for the uncertainty of each $[m_1,\ldots m_N]$ patch, we first diagonalized the [cov **m**] matrix. In this way, we find a new N-dimensional reference system of eigenvectors $[p_1,\ldots, p_N]$ and their relative eigenvalues $[\lambda_{1\ldots}\lambda_N]$. In the eigenvector reference system, eigenvalues describe the axis of an N-dimensional ellipse error with independent values. Finally, we project every λ_i eigenvalue in the $[m_1,\ldots, m_N]$ directions and take, for each m_i direction, the maximum projected value. Although these values don't provide an exhaustive description of the variance/covariance of the **m** vector, they offer a realistic scenario of the uncertainties, shown in Figure B2. It can be seen how the removal of the APS

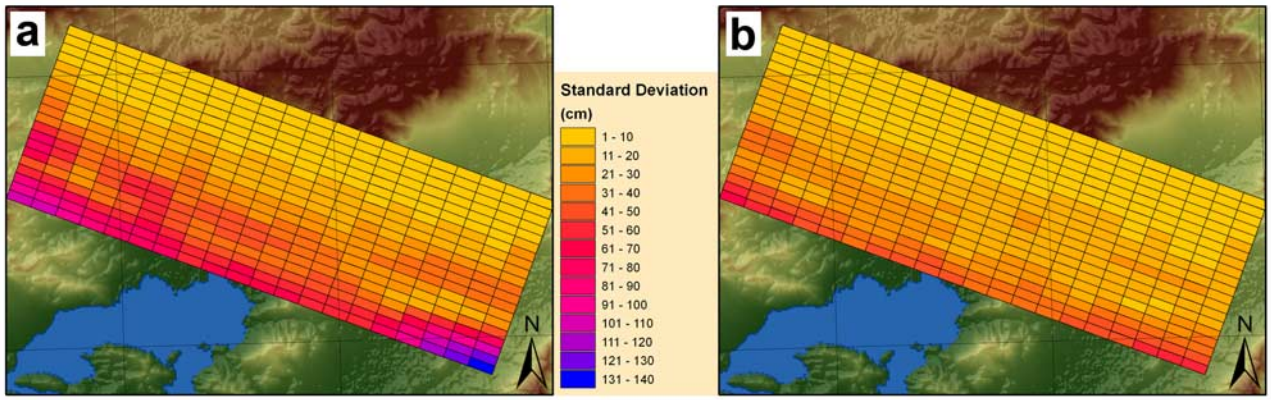

Figure B2. Standard deviation associated to the (a) coseismic and (b) postseismic slip distribution. The increase in precision derives from the APS filtering leading to noise reduction in the observed data, as shown in the time series before and after the filtering in Figure 6.

between the co- and postseismic modeling, lead to an improvement of the precision in the retrieved slip.

[64] **Acknowledgments.** We thank M. Cocco for the suggestions in the postseismic analysis, I. Hunstad for intriguing discussions on the error analysis, Tim Wright for the discussion on DInSAR modeling during S.A. visit to COMET, and S. Monna for the language improvements. Special thanks to the reviewers, in particular, to Paul Lundgren for his care in reading the manuscript and his suggestions. The ESA AO for Greece proposal ID-1454 provided the ERS images. The NOA director provided the aftershock data. We also thank Simpson, Parsons, Drakatos, and Karastathis for discussions. This work was partially funded by MUR, Italy, in the framework of an FIRB project, and the research activity has been partially funded by the Italian Space Agency, SIGRIS project.

References

Assimaki, D., G. Gazetas, and F. Kausel (2005), Effects of local soil conditions on the topographic aggravation of seismic motion: Parametric investigation and recorded field evidence from the 1999 Athens earthquake, *Bull. Seismol. Soc. Am.*, *95*(3), 1059–1089.

Baumont, D., F. Courboulex, O. Scotti, N. Melis, and G. Stavrakakis (2002), Slip distribution of the M_w5.9 1999 Athens earthquake inverted from regional seismological data, *Geophys. Res. Lett.*, *29*(15), 1720, doi:10.1029/2001GL014261.

Baumont, D., O. Scotti, F. Courboulex, and N. Melis (2004), Complex kinematic rupture of the Mw 5.9, 1999 Athens earthquake as revealed by the joint inversion of regional seismological and SAR data, *Geophys. J. Int.*, *158*, 1078–1087.

Berardino, P., G. Fornaro, R. Lanari, and E. Sansosti (2002), A new algorithm for surface deformation monitoring based on small baseline differential SAR interferograms, *IEEE Trans. Geosci. Remote Sens.*, *40*(11), 2375–2383.

Bürgmann, R., S. Ergintav, P. Segall, E. H. Hearn, S. McClusky, R. E. Reilinger, H. Woith, and J. Zschau (2002), Time-dependent distributed afterslip on and deep below the Izmit earthquake rupture, *Bull. Seismol. Soc. Am.*, *92*(1), 126–137.

Casu, F., M. Manzo, and R. Lanari (2006), A quantitative assessment of the SBAS algorithm performance for surface deformation retrieval from DInSAR data, *Remote Sens. Environ.*, *102*(3-4), 195–210.

Crosetto, M., B. Crippa, and E. Biescas (2005), Early detection and in-depth analysis of deformation phenomena by radar interferometry, *Eng. Geol.*, *79*(1–2), 81–91.

Donnellan, A., and G. A. Lyzenga (1998), GPS observation of fault afterslip and upper crustal deformation following the Northridge earthquake, *J. Geophys. Res.*, *103*(B9), 21,285–21,297.

Ferretti, A., C. Prati, and F. Rocca (2000), Non-linear subsidence rate estimation using permanent scatterers in differential SAR interferometry, *IEEE Trans. Geosci. Remote Sens.*, *38*(5), 2202–2212.

Fialko, Y. (2006), Interseismic strain accumulation and the earthquake potential on the southern San Andreas fault system, *Nature*, *441*, 968–971, doi:10.1038/nature0479.

Fielding, E. J., P. Lundgren, G. J. Funning, and R. Bürgmann (2007), Postseismic deformation during three years after the 2003 Bam, Iran earthquake from InSAR time series, *European Geoscience Union 2007*, SRef-ID: 1607-7962/gra/EGU2007-A-05918.

Fornaro, G., F. Serafino, and A. Pauciullo (2007a), Deformation monitoring over a large area via the ESD technique with data takes on adjacent tracks, in *Proc. IEEE Int. Geosci. Remote Sens. Symp.*, IGARSS 2007, pp. 2114–2117, IEEE Int., Barcelona, Spain, doi:10.1109/IGARSS.2007.4423251.

Fornaro, G., A. Pauciullo, and F. Serafino (2007b), Deformation monitoring over large areas with Multipass Differential SAR Interferometry: A new approach based on the use of Spatial Differences, *Int. J. Remote Sen. (IJRS)*, in press.

Funning, G. J., B. Parsons, T. J. Wright, J. A. Jackson, and E. J. Fielding (2005), Surface displacements and source parameters of the 2003 Bam, Iran earthquake from Envisat Advanced Synthetic Aperture Radar imagery, *J. Geophys. Res.*, *110*(B9), B09406, doi:10.1029/2004JB003338.

Gabriel, A. K., R. M. Goldstein, and H. A. Zebker (1989), Mapping small elevation changes over large areas: Differential radar interferometry, *J. Geophys. Res.*, *94*(B7), 9183–9191.

Ganas, A., S. B. Pavlides, S. Sboras, S. Valkaniotis, S. Papaioannou, G. A. Alexandris, A. Plessa, and G. A. Papadopoulos (2004), Active fault geometry and kinematics in Parnitha Mountain, Attica, Greece, *J. Struct. Geol.*, *26*, 2103–2118.

Gazetas, G., P. V. Kallou, and P. N. Psarropoulos (2002), Topography and soil effects in the Ms 5.9 Parnitha (Athens) earthquakes: The case of Adámes, *Nat. Hazards*, *27*(1–2), 133–169.

Goldstein, R. (1995), Atmospheric limitations to repeat-track radar interferometry, *Geophys. Res. Lett.*, *22*(18), 2517–2520.

Hanssen, R. (2001), *Radar Interferometry: Data Interpretation and Error Analysis*, Kluwer Acad., Netherlands.

Harris, R. A. (1998), Introduction to special section: Stress triggers, stress shadows, and implications for seismic hazard, *J. Geophys. Res.*, *103*(B10), 24,347–24,358.

Harris, R. A., and R. W. Simpson (1996), In the shadow of 1857—the effect of the great Ft. Tejon earthquake on subsequent earthquakes in southern California, *Geophys. Res. Lett.*, *23*(3), 229–232.

Hearn, E. H., R. Bürgmann, and R. E. Reilinger (2002), Dynamics of Izmit earthquake postseismic deformation and loading of the Düzce earthquake hypocenter, *Bull. Seismol. Soc. Am.*, *92*, 172–193.

Hooper, A., H. Zebker, P. Segall, and B. Kampes (2004), A new method for measuring deformation on volcanoes and other natural terrains using InSAR persistent scatterers, *Geophys. Res. Lett.*, *31*, L23611, doi:10.1029/2004GL021737.

Hu, Y., K. Wang, J. He, J. Klotz, and G. Khazaradze (2004), Three-dimensional viscoelastic finite element model for postseismic deformation of the great 1960 Chile earthquake, *J. Geophys. Res.*, *109*, B12403, doi:10.1029/2004JB003163.

Husen, S., and E. Kissling (2001), Postseismic fluid flow after the large subduction earthquake of Antofagasta, Chile, *Geology*, *29*, 847–850.

Jonsson, S., H. Zebker, P. Segall, and F. Amelung (2002), Fault slip distribution of the *Mw* 7.2 Hector Mine earthquake estimated from satellite radar and GPS measurements, *Bull. Seismol. Soc. Am.*, *92*, 1377–1389.

Jonsson, S., P. Segall, R. Pederson, and G. Bjornsson (2003), Post-earthquake ground movements correlated to pore-pressure transients, *Nature*, *424*, 179–183.

Kirkpatrick, S., C. D. Gelatt, and M. P. Vecchi (1983), Optimization by simulated annealing, *Science*, *220*, 671–680.

Kontoes, C., P. Elias, O. Sykioti, P. Briole, D. Remy, M. Sachpazi, G. Veis, and I. Kotsis (2000), Displacement field and fault model for the September 7, 1999 Athens earthquake inferred from ERS2 satellite radar interferometry, *Geophys. Res. Lett.*, *27*(24), 3989–3992.

Lanari, R., F. Casu, M. Manzo, G. Zeni, P. Berardino, M. Manunta, and A. Pepe (2007), An overview of the small baseline subset algorithm: A DInSAR technique for surface deformation analysis, *Pure Appl. Geophys.*, *164*, 637–661, doi:10.1007/s00024-007-0192-9.

Lawson, C. L., and R. J. Hanson (1974), *Solving Least Squares Problems*, Prentice-Hall, Englewood Cliffs, N.J.

Li, Z., J. P. Muller, P. Cross, and E. J. Fielding (2005), Interferometric synthetic aperture radar (InSAR) atmospheric correction: GPS, moderate resolution imaging spectroradiometer (MODIS), and InSAR integration, *J. Geophys. Res.*, *110*, B03410, doi:10.1029/2004JB003446.

Louvari, E., and A. Kiratzi (2001), Source parameters of the 7 September 1999 Athens (Greece) earthquake based on teleseismic data, *J. Balkan Geophys. Soc.*, *4*(3), 51–60.

Ma, X. Q., and N. J. Kusznir (1995), Coseismic and postseismic subsurface displacements and strains for a dip-slip normal fault in a three-layer elastic-gravitational medium, *J. Geophys. Res.*, *100*(B7), 12,813–12,830.

Marone, C. J., C. H. Scholz, and R. Bilham (1991), On the mechanics of earthquake afterslip, *J. Geophys. Res.*, *96*(B5), 8441–8452.

Massonnet, D., M. Rossi, C. Carmona, F. Adragna, G. Peltzer, K. Feigl, and T. Rabaute (1993), The displacement field of the Landers earthquake mapped by radar interferometry, *Nature*, *364*, 138–142.

Melini, D., M. Volpe, and A. Piersanti (2006), Finite element modeling of the 2004 giant Sumatra earthquake postseismic displacement field, *Eos Trans. AGU*, Fall Meet., Abstract G33A-0029.

Menke, W. (1984), *Geophysical Data Analysis: Discrete Inverse Theory*, Academic Press, New York.

Mora, O., J. J. Mallorqui, and A. Broquetas (2003), Linear and nonlinear terrain deformation maps from a reduced set of interferometric SAR images, *IEEE Trans. Geosci. Remote Sens.*, *41*, 2243–2253.

Murray, J., and J. Langbein (2006), Slip on the San Andreas Fault at Parkfield, California, over two earthquake cycles, and the implications for seismic hazard, *Bull. Seismol. Soc. Am.*, *96*(4B), S283–S303, doi:10.1785/0120050820.

Nelder, J. A., and R. Mead (1965), A simplex method for function minimization, *Comput. J.*, *7*, 308–313.

Nostro, C., A. Piersanti, and M. Cocco (2001), Normal fault interaction caused by coseismic and postseismic stress changes, *J. Geophys. Res.*, *106*(B9), 19,391–19,410.

Okada, Y. (1985), Surface deformation due to shear and tensile faults in a half-space, *Bull. Seismol. Soc. Am.*, *75*, 1135–1154.

Papadimitriou, P., N. Voulgaris, I. Kassaras, G. Kaviris, N. Delibasis, and K. Makropoulos (2002), The M_w = 6.0, 7 September 1999 Athens earthquake, *Nat. Hazards*, *27*(1–2), 15–33.

Papadopoulos, G. A., G. Drakatos, D. Papanastassiou, I. Kalogeras, and G. Stavrakakis (2000), Preliminary results about the catastrophic earth-

quake of 7 September 1999 in Athens, Greece, *Seismol. Res. Lett.*, *71*(3), 318–329.

Papadopoulos, G. A., A. Ganas, and S. Pavlides (2002), The problem of seismic potential assessment: Case study of the unexpected earthquake of 7 September 1999 in Athens, Greece, *Earth Planets Space*, *54*, 9–18.

Papadopoulos, G. A., H. Matsumoto, A. Ganas, V. Karastathis, and S. B. Pavlides (2004), Deformation patterns associated with the M5.9 Athens (Greece) earthquake of 7 September 1999, *J. Seismol.*, *8*, 381–394.

Parsons, B., T. J. Wright, P. Rowe, J. Andrews, J. Jackson, R. Walker, M. Khatib, M. Talebian, E. Bergman, and E. R. Engdahl (2006), The 1994 Sefidabeh (eastern Iran) earthquakes revisited: New evidence from satellite radar interferometry and carbonate dating about the growth of an active fold above a blind thrust fault, *Geophys. J. Int.*, *164*(1), 202–217, doi:10.1111/j.1365-246X.2005.02655.x.

Pavlides, S. B., G. A. Papadopoulos, and A. Ganas (2002), The fault that caused the Athens September 1999 Ms = 5.9 earthquake: Field observations, *Nat. Hazards*, *27*(1–2), 61–85.

Pepe, A., and R. Lanari (2006), On the extension of the minimum cost flow algorithm for phase unwrapping of multitemporal differential SAR interferograms, *IEEE Trans. Geosci. Remote Sens.*, *44*(9), 2374–2383.

Pollitz, F. F., R. Bürgmann, and P. Segall (1998), Joint estimation of afterslip rate and postseismic relaxation following the 1989 Loma Prieta earthquake, *J. Geophys. Res.*, *103*(B11), 26,975–26,992.

Roumelioti, Z., A. Kiratzi, N. Theodoulidis, I. Kalogeras, and G. Stavrakakis (2003), Rupture directivity during the September 7, 1999 (Mw 5.9) Athens (Greece) earthquake inferred from forward modeling of strong ground motion, *Pure Appl. Geophys.*, *160*(12), 2301–2318.

Rundle, J. B., and D. D. Jackson (1977), Numerical simulation of earthquake sequences, *Bull. Seismol. Soc. Am.*, *67*, 1363–1377.

Ryder, I., B. Parsons, T. J. Wright, and G. J. Funning (2007), Post-seismic motion following the 1997 Manyi (Tibet) earthquake: InSAR observations and modelling, *Geophys. J. Int.*, *169*, 1009–1027.

Sargeant, S. L., P. W. Burton, A. Douglas, and J. R. Evans (2002), The source mechanism of the Athens earthquake, September 7, 1999, estimated from P seismograms recorded at long range, *Nat. Hazards*, *27*, 35–45.

Savage, J. C. (1990), Equivalent strike-slip earthquake cycles in half-space and lithosphere-asthenosphere Earth models, *J. Geophys. Res.*, *95*(B4), 4873–4879.

Savage, J. C., and W. H. Prescott (1978), Asthenosphere readjustment and the earthquake cycle, *J. Geophys. Res.*, *83*(B7), 3369–3376.

Shen, Z. K., D. D. Jackson, Y. Feng, M. Cline, M. Kim, P. Fang, and Y. Bock (1994), Postseismic deformation following the Landers earthquake, California, 28 June 1992, *Bull. Seismol. Soc. Am.*, *84*(3), 780–791.

Simpson, R. W., and P. A. Reasenberg (1994), Earthquake-induced static-stress changes on Central California faults, the Loma Prieta, California, earthquake of October 17, 1989—tectonic processes and models, *U.S. Geol. Surv.*, *Prof. Pap. 1550-F*, 55–89.

Stavrakakis, G. N., G. Chouliara, and G. Panopoulou (2002), Seismic source parameters for the ML = 5.4 Athens earthquake (7 September 1999) from a new telemetric broad band seismological network in Greece, *Nat. Hazards*, *27*, 47–60.

Tselentis, G. A. J., and Zahradnik (2000), The Athens earthquake of 7 September, 1999, *Bull. Seismol. Soc. Am.*, *90*(5), 1143–1160.

Usai, S. (2003), A least squares database approach for SAR interferometric data, *IEEE Trans. Geosci. Remote Sens.*, *41*(4), 753–760.

Werner, C., U. Wegmuller, T. Strozzi, and A. Wiesmann (2003), Interferometric point target analysis for deformation mapping, *Proc. IGARSS*, *7*, 4362–4364.

Wright, T. J., Z. Lu, and C. Wicks (2003), Source model for the Mw 6.7, 23 October 2002, Nenana Mountain Earthquake (Alaska) from InSAR, *Geophys. Res. Lett.*, *30*(18), 1974, doi:10.1029/2003GL018014.

S. Atzori and S. Salvi, Remote Sensing Laboratory, Istituto Nazionale di Geofisica e Vulcanologia, Sezione di Roma, Via di Vigna Murata 605, I-00143 Rome, Italy. (atzori@ingv.it)

G. Fornaro and M. Manunta, Istituto per il Rilevamento Elettromagnetico dell'Ambiente, National Research Council, Via Diocleziano 328, Naples I-80124, Italy.

A. Ganas, Institute of Geodynamics, National Observatory of Athens, Lofos Nymfon, P.O. Box 20048, GR-11810 Athens, Greece.